JACS
JOURNAL OF THE AMERICAN CHEMICAL SOCIETY
pubs.acs.org/JACS
Article

Construction of Zeolite Framework-Anchored Rh−$(O−Zn)_x$ Sites for Ethylene Hydroformylation

Haocheng Hu, Wenhao Cui, Mingbin Gao, Linying Wang, Shiping Liu, Liang Qi,* Wenfu Yan, Peng Tian,* and Zhongmin Liu*

Cite This: J. Am. Chem. Soc. 2025, 147, 34381−34394
Read Online
ACCESS | Metrics & More | Article Recommendations | Supporting Information

ABSTRACT: Zeolite-confined Rh-based catalysts have emerged as promising heterogeneous candidates for olefin hydroformylation. However, they face challenges of reactant- and product-induced Rh leaching and aggregation. Herein, zeolite framework-anchored $Rh^{\delta+}-(O-Zn)_x$ sites were designed and are shown to have remarkable activity and stability for gas-phase ethylene hydroformylation. The bimetallic catalysts were synthesized by coencapsulating Rh and Zn species into Silicalite-1 zeolite, and the $Rh^{\delta+}-(O-Zn)_x$ sites were *in situ* constructed during the induction period of the hydroformylation process through the interaction between mobile Rh-carbonyl species and framework ≡SiOZn−O(H). The change of the Zn/Rh molar ratio significantly affects the dispersion of Rh and the proportion of highly active $Rh^{\delta+}$. The optimal $0.2Rh@Zn_3$-S-1 catalyst achieves a propanal turnover frequency as high as 148 h^{-1} at 363 K and shows no sign of deactivation during the 40 h test. In contrast, zinc-free 0.2Rh@S-1 suffers rapid deactivation due to Rh aggregation. *In situ* Fourier transform infrared (FTIR) spectroscopy reveals that the transfer desorption of propanal from Rh to Zn−O contributes to the redispersion of Rh during the construction of $Rh^{\delta+}-(O-Zn)_x$ structures. Moreover, the observed $HRh(CO)_2$ species together with the enrichment of $Rh^{\delta+}$-propionyl intermediates on the catalyst indicates that the hydrogenation of acyl species is the rate-limiting step of ethylene hydroformylation, which is further supported by kinetic analysis. This study presents a new strategy for designing stable and efficient gas-phase ethylene hydroformylation catalysts using zeolite-anchored metal species as inorganic ligands for $Rh^{\delta+}$ centers and provides insights into the hydroformylation mechanism occurring on the bimetallic sites.

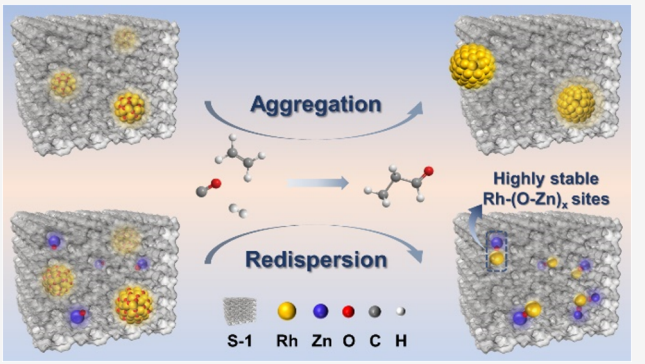

1. INTRODUCTION

The hydroformylation reaction is one of the most important industrial processes to produce aldehydes from alkenes and syngas, with an annual production scale for more than 24 million metric tons.[1−5] Currently, the majority of propanal, butanal, and other linear aldehydes with a world annual productivity of over 1 million, over 10 million, and over 2.4 million are produced via olefin hydroformylation over homogeneous Rh−P complex catalysts.[2,6−9] However, the homogeneous process brings about unavoidable challenges in catalyst separation and recovery, which causes loss of precious metals and discharge of phosphorus-containing wastes.[10−12] These limitations motivated the development of heterogeneous catalysts, such as Rh-supported phosphine-modified porous organic polymers (Rh-POPs),[13,14] solid Rh phosphides,[15,16] and Rh complexes dispersed in the supported ionic liquid.[17] Nonetheless, most of these catalysts still need phosphine ligands, which are usually expensive and air/moisture-sensitive.[18,19]

To solve problems from organic phosphine ligands, research efforts have been devoted to developing Rh-based hydroformylation catalysts utilizing low-cost and eco-friendly promoters.[20−27] Promising promoters tested to date include inorganic phosphorus, nonprecious transition metals, and metal oxides. Meanwhile, the creation of dispersed Rh sites with a well-tuned electronic property[5,24,28] has been recognized to be critical for achieving an efficient hydroformylation performance. For instance, Liu et al. reported that the ethylene hydroformylation activity of Rh−0.5P supported on SiO_2 was enhanced by more than 3 times compared to Rh/SiO_2 due to the modification effect from the P promoter in the Rh geometric and electronic property.[29] Chen et al. revealed that Rh−Co bimetallic formation in $RhCo_3$/MCM-22 facilitated the production of C3 oxygenates in ethylene hydroformylation.[30] Huang et al. reported that Zn-promoted Rh−Zn

Received: May 6, 2025
Revised: September 1, 2025
Accepted: September 2, 2025
Published: September 10, 2025

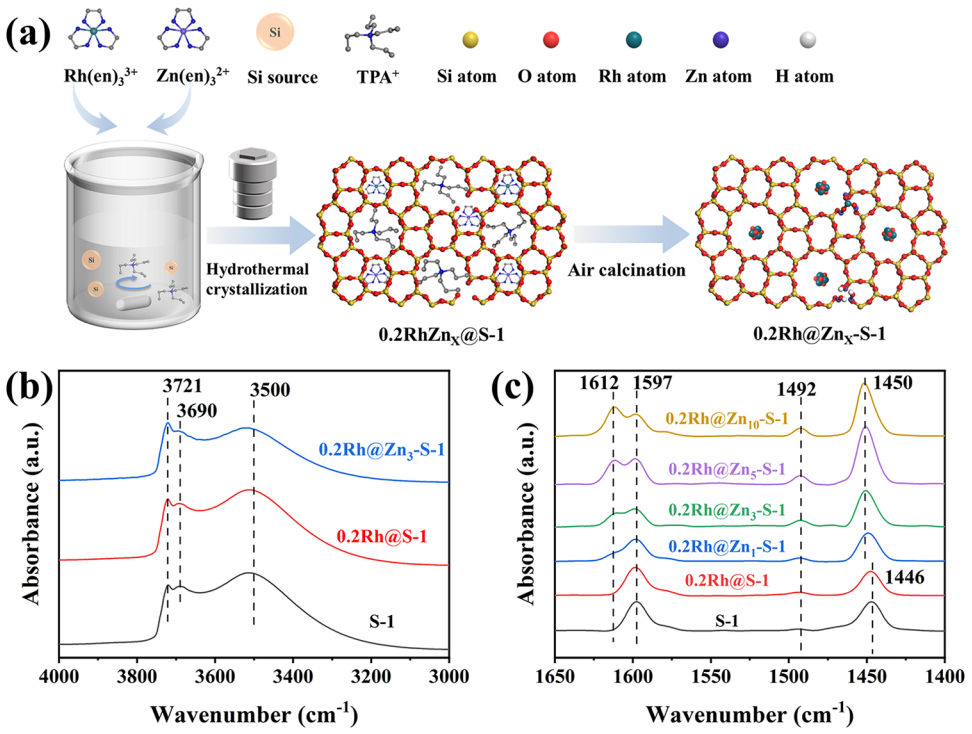

Figure 1. (a) Schematic illustration of the preparation of 0.2Rh@Zn_x-S-1 samples. (b) Comparison of the FTIR spectra in the hydroxyl vibration region of S-1, 0.2Rh@S-1, and 0.2Rh@Zn_3-S-1. (c) Comparison of the pyridine-adsorbed FTIR spectra of S-1, 0.2Rh@S-1, and 0.2Rh@Zn_x-S-1 (x = 1, 3, 5, and 10).

nanoparticles supported on SBA-15 showed higher activity than Rh/SBA-15 for styrene hydroformylation, and only the exposed Rh−Zn bimetallic sites on the edges of particles served as active centers.[31] Christopher et al. constructed atomically dispersed Rh−WO_x pairs over γ-Al_2O_3 with boosted ethylene hydroformylation activity and selectivity due to the enrichment of ethylene over WO_x and H_2 dissociation at the Rh−WO_x interface.[22] Bell et al. grafted Rh into nests of ≡SiOZn−O_x or ≡SiOCo−O_x groups prepared in dealuminated zeolite BEA and found that ethylene hydroformylation was catalyzed by atomically dispersed Rh species, which was influenced by Rh−Metal interactions. The hydroformylation activity of the Rh−Co system surpassed that of the Rh−Zn counterpart.[5]

The above examples explored the dispersion as well as the electronic modulation effect over Rh from secondary metal species. For the metal@zeolite material, it should be noted that the effective dispersion and electronic modulation effect over metals can also be achieved from zeolite framework-associated local environments. Recently, a series of studies have reported the utilization of the zeolite framework for metal dispersion, especially through an *in situ* encapsulation method.[32−36] The zeolite can confine and disperse Rh atoms, and its framework ≡Si−O^-, as an inorganic crystal ligand, can coordinate with $Rh^{\delta+}$, therefore creating highly dispersed Rh centers with a tuned electronic property for hydroformylation. For example, Shang et al. have reported that isolated $Rh^{\delta+}$ encaged in faujasite exhibited high catalytic activity, perfect chemoselectivity, and recyclability in 1-hexene hydroformylation.[36] Yu et al. prepared the Rh_1@S-1 (where S-1 denotes Silicalite-1 with an MFI structure) catalyst through *in situ* synthesis followed by direct H_2 reduction treatment.[32] $Rh^{\delta+}$ single atoms were revealed to be the active centers for ethylene hydroformylation. After the optimization of reaction conditions and the reaction atmosphere, the catalyst exhibited a propanal turnover frequency (TOF) of ca. 86 h^{-1} at 353 K and 4.0 MPa pressure, with a feed gas composition of $C_2H_4/CO/H_2$ = 1:1:1. Recently, Corma et al. reported that the Rh^{3+} sites confined in MFI zeolite, stabilized by phosphate species through Rh−O−P interactions, exhibited improved activity for ethylene hydroformylation, achieving an initial TOF of 70 h^{-1} at 363 K and 1.0 MPa pressure.[35] However, gradual deactivation was still observed under prolonged reaction conditions.

The observed promoter effects by secondary metals or zeolite frameworks inspired us to imagine whether a zeolite framework could be utilized to confine highly dispersed Rh-based bimetallic centers, where the property of Rh can be modulated by both the secondary metal and the zeolite framework. While this concept has been investigated for alkane dehydrogenation catalysts,[37−45] its application to hydroformylation remains unexplored. Herein, we synthesized siliceous MFI zeolite-encapsulated Rh and Zn bimetallic catalysts via a facile ethylenediamine-ligand protection strategy. The best 0.2Rh@Zn_3-S-1 catalyst, obtained by optimizing the Zn/Rh ratio, exhibited superior catalytic activity and stability in gas-phase ethylene hydroformylation, as compared with 0.2Rh@S-1. To elucidate the outstanding catalytic performance and the induction period observed for 0.2Rh@Zn_3-S-1, the Rh dispersion and structural evolution during the hydroformylation reaction were investigated by X-ray absorption spectroscopy (XAS), Fourier transform infrared (FTIR) spectroscopy, scanning transmission electron microscopy (STEM), and molecular dynamics (MD) simulation. The *in situ* formation of Rh−$(O−Zn)_x$ active sites during the induction period was revealed, which evidently improved the electronic and structural stability of highly dispersed $Rh^{\delta+}$, a necessary status for achieving high hydroformylation activity and selectivity. Our findings provide inspiration for the design

https://doi.org/10.1021/jacs.5c07586
J. Am. Chem. Soc. 2025, 147, 34381−34394

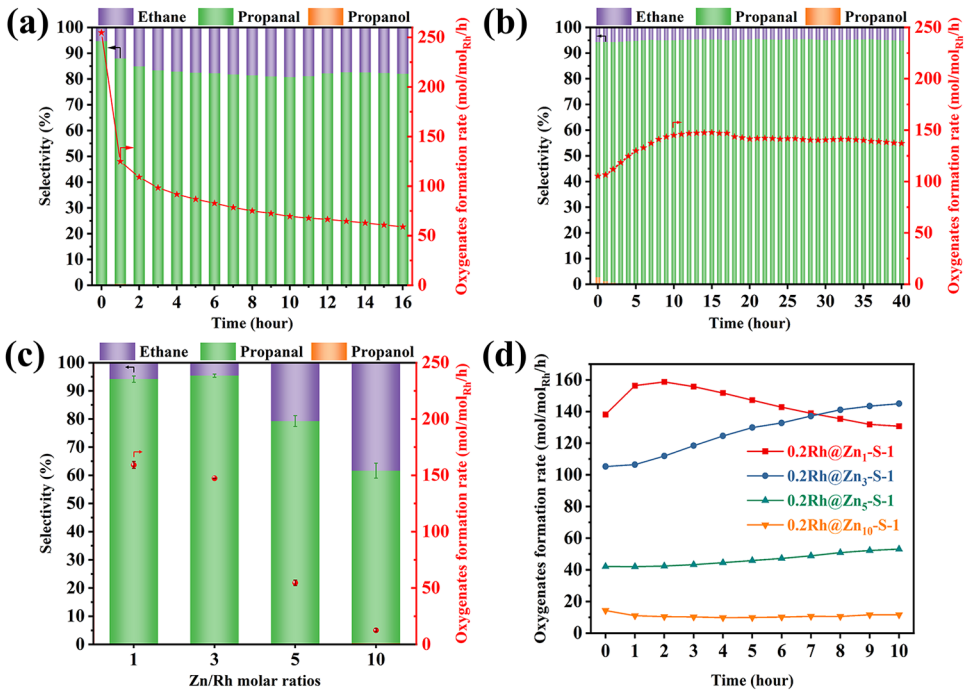

Figure 2. Gas-phase ethylene hydroformylation over (a) 0.2Rh@S-1 and (b) 0.2Rh@Zn$_3$-S-1. (c) Comparison of ethylene hydroformylation activity and selectivity over 0.2Rh@Zn$_x$-S-1 with different Zn/Rh molar ratios (for Zn/Rh = 1, TOS = 2 h; for Zn/Rh = 3, TOS = 15 h; for Zn/Rh = 5/10, TOS = 10 h). Error bars correspond to the standard deviations from three parallel evaluations. (d) Comparison of the catalytic stability of 0.2Rh@Zn$_x$-S-1. Reaction conditions: 200 mg of the catalyst, 363 K, 1 MPa, a feed flow of 1C$_2$H$_4$/1H$_2$/1CO (30 mL(NTP)/min).

and mechanism understanding of heterogeneous hydroformylation catalysts with bimetallic active sites anchored on the zeolite framework.

2. RESULTS AND DISCUSSION

2.1. Synthesis and Characterization of the 0.2Rh@Zn$_x$-S-1 Sample. As shown in Figure 1a, an ethylenediamine-ligand protection strategy was used for the *in situ* encapsulation of Rh and Zn species into the Silicalite-1 (S-1) zeolite. Ethylenediamine played an important role in maintaining both a high dispersion and a high encapsulation degree of Rh species, while synthesis utilizing other ammonia/amine failed, which can be reflected from the comparative experiments of encapsulating Rh and Zn species using different ammonia/amine (see Note S1, Figures S5−S8 and Table S2 for more details). The obtained solid products were calcined in a dry air flow to remove organics and named 0.2Rh@Zn$_x$-S-1 (wherein 0.2 and x represent the weight loading of Rh and the molar ratio of Zn/Rh in the samples, respectively). For comparison, the sample without Rh/Zn introduction (named S-1) and the sample with only Rh introduction (named 0.2Rh@S-1) were prepared through the same procedure. The scanning electron microscopy (SEM) images of the samples (Figure S1) show the typical hexagonal crystal morphology, characteristic of the MFI-type zeolite.[46,47] Inductively coupled plasma optical emission spectrometry (ICP-OES) analyses (Table S1) demonstrate that the amounts of Rh and Zn in the samples are almost the same as those added in the synthesis gel, proving the success of the one-pot introduction of Rh and Zn species into zeolites. X-ray diffraction (XRD) patterns of the samples (Figure S2) exhibit characteristic MFI-type zeolite frameworks with a high crystallinity. No patterns attributed to metal/metal oxide particles can be observed, which should be attributed to the low metal content of the samples (see Note S2, Figures S9−S10 for more details). N_2 physisorption measurements reveal comparable BET surface areas and micropore volumes for 0.2Rh@Zn$_x$-S-1, 0.2Rh@S-1 and S-1 samples (Figure S3 and Table S1).

Ultraviolet−visible (UV−vis) and Fourier transform infrared (FTIR) spectroscopies were utilized to probe the interactions between encapsulated metal species and the zeolite framework. The absence of absorption bands in the 300−400 nm range in the UV−vis spectra (Figure S4) confirms the lack of large, oxidized metal nanoparticles.[48,49] A distinct peak at ∼202 nm is observed for 0.2Rh@S-1, attributed to the charge transfer between Rh and lattice O^{2-} within the zeolite framework.[47,50,51] For 0.2Rh@Zn$_x$-S-1 samples, a more evident charge transfer is observed from Zn species, and the intensity of the absorption signal at 202 nm increases rapidly with the incremental Zn/Rh ratios from 1 to 10.

FTIR spectra of the hydroxyl vibration region of the samples are shown in Figure 1b. For S-1 zeolite, three bands at 3721, 3690, and 3500 cm^{-1} are observed, corresponding to the internal isolated silanol, adjacent silanol, and silanol nests, respectively.[52−54] A similar spectrum is observed for 0.2Rh@S-1, while for 0.2Rh@Zn$_3$-S-1, the relative intensity of the band at 3500 cm^{-1} decreases obviously, implying the consumption of silanol nests due to the formation of the Si−O−Zn bond.[58−62] Pyridine-adsorbed FTIR spectra of the samples are shown in Figure 1c. For the S-1 sample, two prominent bands appear at 1597 and 1446 cm^{-1}, attributed to pyridine bound to hydrogen-bonded silanol nests.[5,51,55−57] With the introduction of Rh species, the intensity of the bands remains unchanged, suggesting a weak interaction between Rh species and silanol nests. However, for Rh- and Zn-coencapsulated samples, two new bands emerge at 1612 and 1450 cm^{-1}, assigned to pyridine interacting with Zn Lewis acid sites (Si−O−Zn−O).[5,56,57] Note that the band at 1492 cm^{-1} is generally

https://doi.org/10.1021/jacs.5c07586
J. Am. Chem. Soc. 2025, 147, 34381−34394

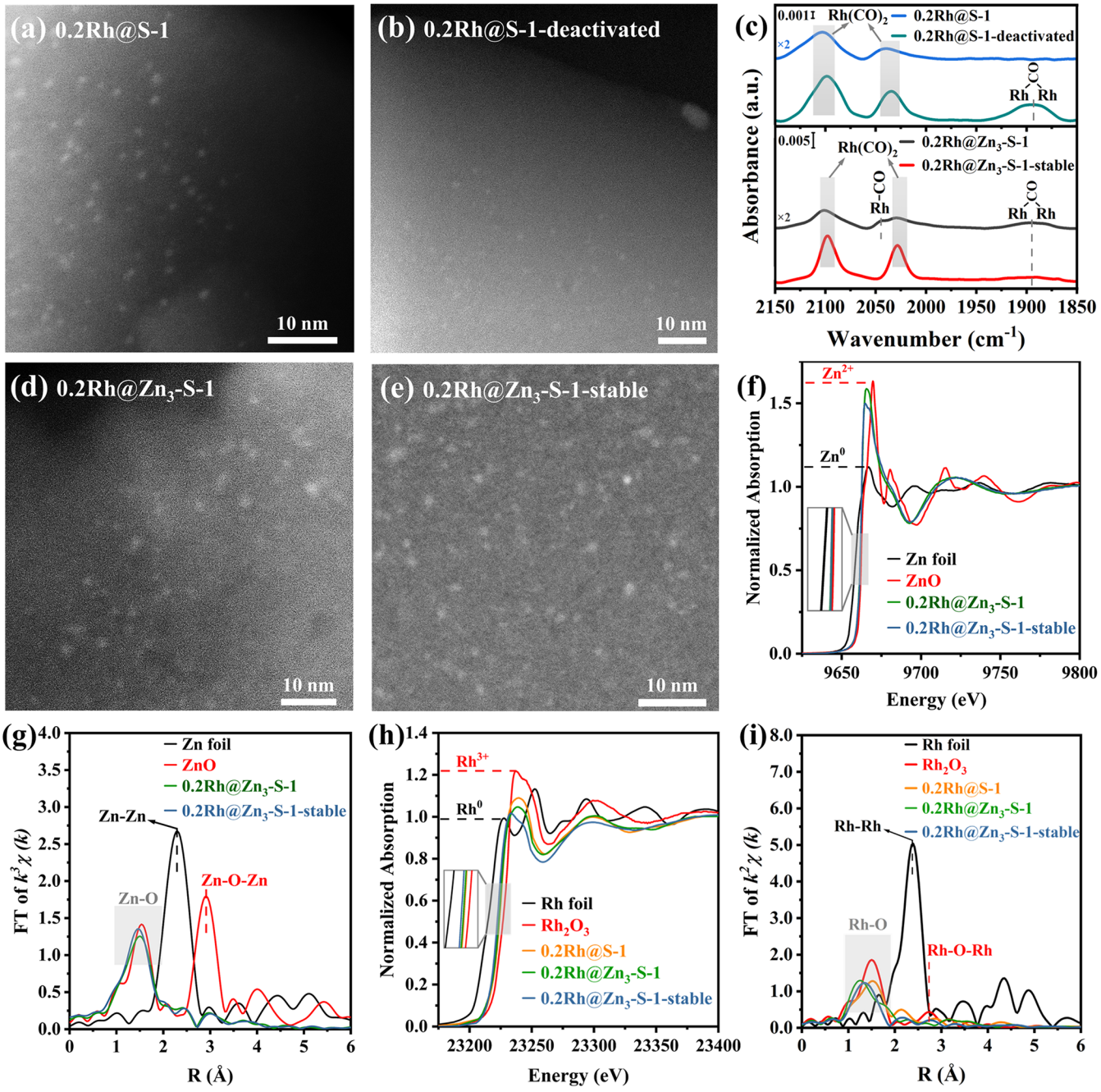

Figure 3. HAADF-STEM images of (a) 0.2Rh@S-1, (b) 0.2Rh@S-1-deactivated, and (c) CO-adsorbed FTIR spectra collected at 298 K for 0.2Rh@S-1, 0.2Rh@S-1-deactivated, 0.2Rh@Zn_3-S-1, and 0.2Rh@Zn_3-S-1-stable. HAADF-STEM images of (d) 0.2Rh@Zn_3-S-1 and (e) 0.2Rh@Zn_3-S-1-stable. (f) Normalized Zn K-edge XANES spectra, (g) k^3-weighted Zn K-edge EXAFS spectra, (h) normalized Rh K-edge XANES spectra, and (i) k^2-weighted Rh K-edge EXAFS spectra of 0.2Rh@S-1, 0.2Rh@Zn_3-S-1, 0.2Rh@Zn_3-S-1-stable, and reference samples (without phase correction). Reaction conditions: 200 mg of the catalyst, 363 K, 1 MPa, a feed flow of $1C_2H_4/1H_2/1CO$ (30 mL(NTP)/min).

characteristic of both Brønsted and Lewis acid sites.[49] Its absence in pure-silica S-1, combined with the lack of framework Al (and thus Brønsted acidity) in 0.2Rh@Zn_x-S-1, confirms its exclusive origin from the Zn Lewis acid sites. The relative intensity of these bands increases as the Zn/Rh molar ratio increases (from 1 to 10), demonstrating the increase of grafted Zn species.

2.2. Ethylene Hydroformylation Performance of 0.2Rh@Zn_x-S-1. The gas-phase ethylene hydroformylation reaction was evaluated at 363 K and 1 MPa with a feed composition of $C_2H_4/H_2/CO$ = 1:1:1 (Figure 2). For 0.2Rh@S-1 (Figure 2a), the initial oxygenate formation rate was 255 mol/(mol_{Rh}·h) and the selectivity for hydroformylation was 95% (5% ethane byproduct from ethylene hydrogenation). The values surpass those of all reported Rh-based catalysts supported over silica or zeolites under similar test conditions.[35] However, the hydroformylation activity exhibits a rapid decay, decreasing to 125 mol/(mol_{Rh}·h) (88% selectivity) at 1 h and further to 60 mol/(mol_{Rh}·h) (82% selectivity) after 16 h. In contrast to 0.2Rh@S-1, 0.2Rh@Zn_3-S-1 shows an induction period of ~10 h with gradually increased activity (Figure 2b), after which a stable oxygenate formation rate (138−148 mol/

https://doi.org/10.1021/jacs.5c07586
J. Am. Chem. Soc. 2025, 147, 34381−34394

(mol_{Rh}·h)) and selectivity (95%) are achieved and kept stabilized throughout the 40 h test.

It is noted that the activation procedure significantly affects the catalytic performance of both 0.2Rh@S-1 and 0.2Rh@Zn_3-S-1. Compared with the catalysts directly activated in the air flow (Figure 2), those activated by H_2 reduction exhibit an obvious decline in hydroformylation activity (Figure S11). Consequently, a simple air-flow calcination protocol is adopted for catalyst activation in this work.

The ethylene hydroformylation performance over 0.2Rh@Zn_x-S-1 with different Zn/Rh ratios was further investigated and the results are displayed in Figure 2c. As the Zn/Rh ratios increase from 1 to 10, the oxygenate formation rate drops from 159 to 13 mol/(mol_{Rh}·h). The selectivity remains almost unchanged in a range of 94−96% as the Zn/Rh ratio increases from 1 to 3 but decreases rapidly to 61% at Zn/Rh = 10. The catalytic stability tests of the catalysts are shown in Figure 2d. Obviously, the stability of the catalysts increases with the elevated Zn/Rh molar ratio; however, the activity shows a dramatic decrease, and the induction period becomes longer.

It has been reported that Rh-catalyzed hydroformylation activity is sensitive to the dispersion and coordination environments of Rh species, as these factors govern the electronic properties of catalytic centers.[5,22,35] The above reaction results indicate that the coencapsulated Zn species significantly modulate the catalytic activity, selectivity, and stability of the Rh-based catalysts. The gradually improved hydroformylation activity for 0.2Rh@Zn_3-S-1 during the induction period may suggest the generation of new Zn-related Rh-active centers, likely involving the variation of Rh dispersion or the reconstruction of Rh coordination environments.[25,63,64] Characterization techniques, including X-ray photoelectron spectroscopy (XPS) and CO probe molecule FTIR spectroscopy, were further employed to study the 0.2Rh@Zn_x-S-1 catalysts (see Note S3, Figures S12−S15 and Table S3 for more details). The results reveal that the change in the Zn/Rh molar ratio leads to a significant difference in the Rh dispersion and oxidation state, which should be the main reason for the distinct hydroformylation behavior across the catalysts.

2.3. Evolution of Rh Dispersion and Coordination Environments on 0.2Rh@Zn_3-S-1 and 0.2Rh@S-1 during Ethylene Hydroformylation. The evolution of Rh species dispersion was investigated through comparative analyses of the fresh and postreaction catalysts. The optimal 0.2Rh@Zn_3-S-1 catalysts including the fresh and steady-state counterparts (after 40 h reaction, named 0.2Rh@Zn_3-S-1-stable) were selected for characterization. Moreover, fresh 0.2Rh@S-1 and its deactivated counterpart (after 16 h reaction, named 0.2Rh@S-1-deactivated) were also characterized for comparison.

ICP-OES results demonstrate that the catalysts did not lose any metal species after the ethylene hydroformylation reaction (Table S4). Energy-dispersive spectroscopy (EDS) elemental mapping shows the uniform dispersion of metal species in fresh 0.2Rh@S-1 and 0.2Rh@Zn_3-S-1 (Figures S16−S17).

The HAADF-STEM images further reveal that 0.2Rh@S-1 possesses subnanometric Rh_2O_3 clusters with an average particle size of 0.9 nm (Figures 3a and S18), contrasting with larger Rh nanoclusters (1.9−2.1 nm) in 0.2Rh@Zn_3-S-1 (Figures 3d and S20). For 0.2Rh@S-1-deactivated, Rh aggregates (>3 nm) located at the external surface of the crystal (Figures 3b and S19) are observed. Interestingly, 0.2Rh@Zn_3-S-1-stable shows a remarkable Rh redispersion (0.9−1.3 nm, Figures 3e and S21). Furthermore, the microenvironments of Rh species were investigated by EDS line-scan analysis (Figure S22). For 0.2Rh@Zn_3-S-1, the Zn K-line signal shows a uniform intensity around the Rh species. However, after redispersion, an enriched Zn K-line signal around the Rh species can be observed for 0.2Rh@Zn_3-S-1-stable, indicating that the redispersed Rh species prefer to locate near the Zn species.

The structural evolution of Rh species was also investigated by CO-adsorbed FTIR spectroscopy (Figure 3c). The spectrum of 0.2Rh@S-1 exhibits two bands at 2103 and 2039 cm^{-1}, characteristic of asymmetric and symmetric stretching modes of isolated $Rh(CO)_2$ complexes,[65,66] confirming the high dispersion of Rh species. For 0.2Rh@S-1-deactivated, the bands representing $Rh(CO)_2$ undergo a 5−8 cm^{-1} red shift[67,68] with a concurrent emergence of the band at 1894 cm^{-1} attributed to bridged CO on Rh nanoparticles,[69,70] indicative of Rh aggregation. The spectrum of 0.2Rh@Zn_3-S-1 displays four bands centered at 2100, 2030, 2045, and 1891 cm^{-1}. The new band at 2045 cm^{-1} corresponds to linearly adsorbed CO on Rh clusters.[67] Remarkably, for 0.2Rh@Zn_3-S-1-stable, the band at 2045 cm^{-1} vanishes and the bands at 2097 and 2028 cm^{-1} intensify relative to the band at 1891 cm^{-1}, suggesting the reaction-induced Rh redispersion. The spectral evolution aligns with the HAADF-STEM observations. Therefore, it is deduced that the distinct catalytic performance of 0.2Rh@Zn_3-S-1 might be associated with the Rh redispersion during the reaction, which occurs due to the existence of Zn species. X-ray absorption spectroscopy (XAS) was further performed to investigate the structure and coordinative information on Rh and Zn species in 0.2Rh@S-1 and 0.2Rh@Zn_3-S-1. The oxidation state of Zn species in fresh and stable-state 0.2Rh@Zn_3-S-1 was probed by XANES at the Zn K-edge. The spectra of both catalysts were characterized by the prominent white line and edge energy, which are similar to that of Zn^{2+} in the ZnO reference sample (Figure 3f). The real-space EXAFS spectra (Figure 3g) as well as the wavelet-transform EXAFS spectra (Figure S23) of these two catalysts exhibit a similar distance of the Zn−O scattering path at around 1.5 Å, while the Zn−Zn (at around 2.3 Å) and Zn−O−Zn scattering paths (at around 3.0 Å) do not appear in a higher shell range. These results illustrate that all of the Zn species in 0.2Rh@Zn_3-S-1 and 0.2Rh@Zn_3-S-1-stable are highly dispersed by silanol nests through Zn−O−Si bonds without the generation of ZnO_x clusters.[71−74]

The Rh *K*-edge XANES spectra are shown in Figure 3h. Both 0.2Rh@S-1 and 0.2Rh@Zn_3-S-1 present a similar rising edge energy relative to Rh_2O_3, indicating that the encapsulated Rh atoms in both catalysts are with an oxidation state of ca. +3. However, compared with 0.2Rh@S-1, 0.2Rh@Zn_3-S-1 has a lower white line peak intensity as well as absorption edge energy, indicating the relatively low valence state of Rh in 0.2Rh@Zn_3-S-1.[51] For 0.2Rh@Zn_3-S-1-stable, the XANES spectrum displays a further decrease in the intensity of the white line and a slight shift in the absorption edge toward the lower-energy side.

The real-space Rh K-edge EXAFS spectra and the corresponding wavelet-transform spectra for the investigated samples are shown in Figures 3i and S24. No Rh−Rh scattering path (at 2.4 Å) is observed, and all of the three catalysts present a dominant presence of the Rh−O scattering path (in the 1−2 Å range). For 0.2Rh@S-1, the Rh−O−Rh scattering path in a higher shell range (2.7 Å) shows only a

https://doi.org/10.1021/jacs.5c07586
J. Am. Chem. Soc. 2025, 147, 34381−34394

Scheme 1. Structural Evolution of Rh Species Induced by CO in 0.2Rh@Zn_3-S-1 (Taking Rh−$(O−Zn)_3$ Sites and Rh $(CO)_2$ Species as Examples to Illustrate the Evolution Process).

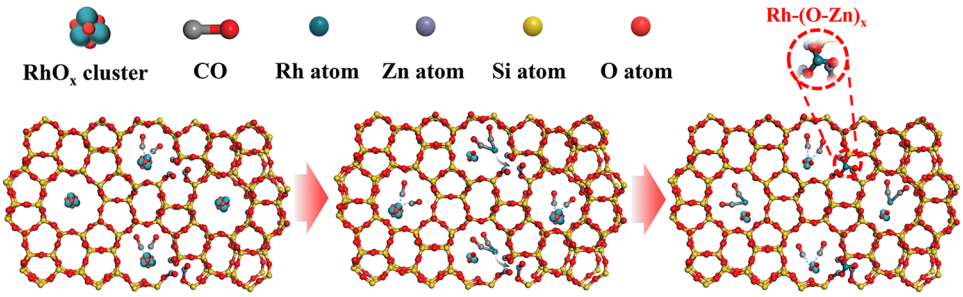

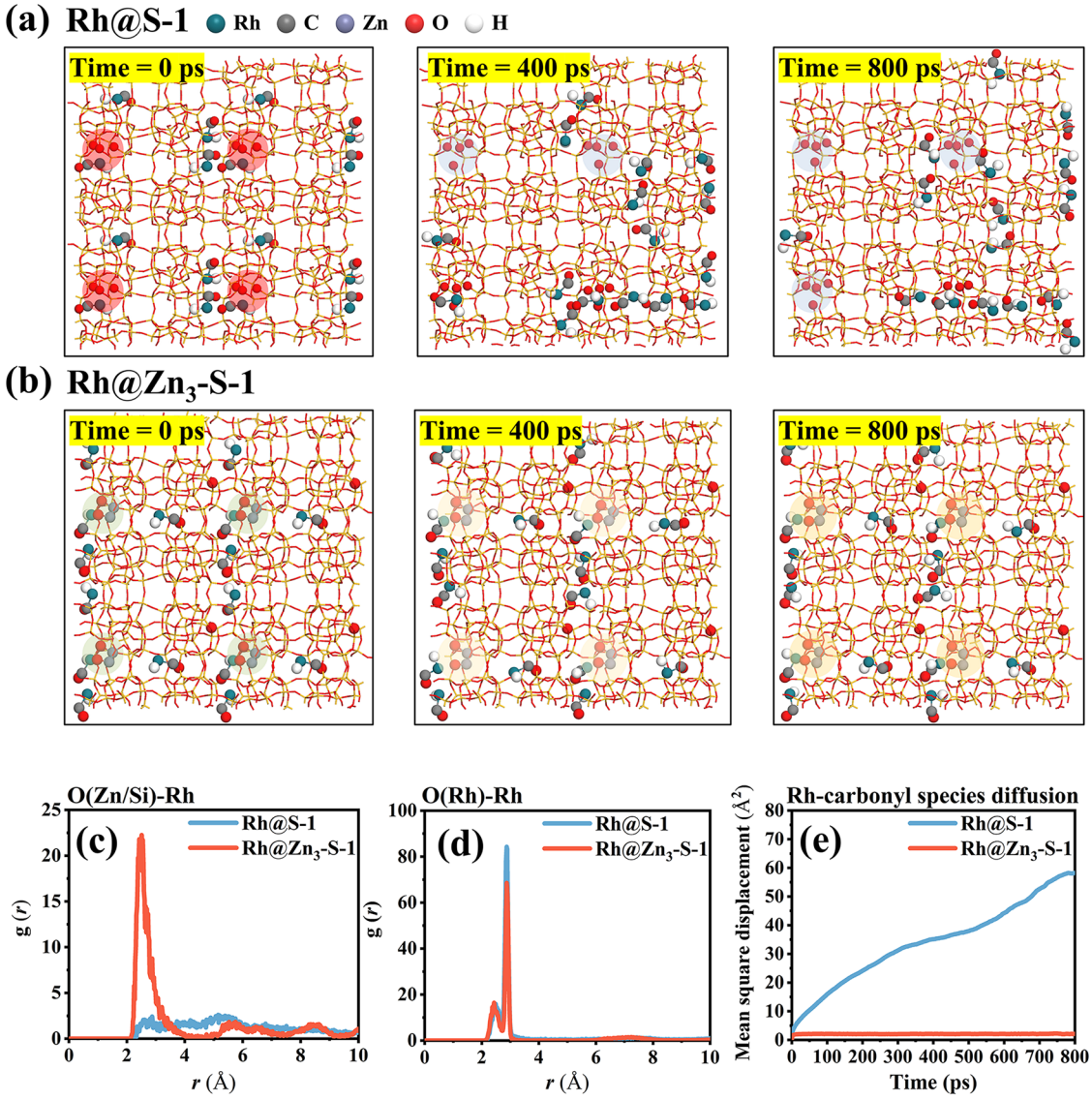

Figure 4. MD simulation of the movement of Rh-carbonyl species in (a) Rh@S-1 and (b) Rh@Zn_3-S-1 at 363 K (the Si−O structure of the MFI framework is highlighted in a red/blue circle; the Zn−O bond grafted by silanol is highlighted in a green/yellow circle). Radial distribution functions for (c) O(Zn/Si)−Rh and (d) O(Rh)−Rh in Rh@S-1 and Rh@Zn_3-S-1. (e) Mean square displacement−time curves of Rh-carbonyl species in Rh@S-1 and Rh@Zn_3-S-1.

weak signal compared with Rh_2O_3, demonstrating the high dispersion of RhO_x species in the fresh catalyst.[35] Interestingly, for 0.2Rh@Zn_3-S-1, there are two distinct Rh−O scattering paths observed at the first shell, with one located at around 1.3 Å and the other one located at around 1.5 Å. Compared with the Rh_2O_3 reference sample, the significant shift of the Rh−O scattering path suggests that new kinds of Rh−O interactions exist in 0.2Rh@Zn_3-S-1. Moreover, for the Rh−O signal identified in the 0.2Rh@Zn_3-S-1-stable catalyst, there is only one peak appearing at around 1.3 Å, indicating that the

https://doi.org/10.1021/jacs.5c07586
J. Am. Chem. Soc. 2025, 147, 34381−34394

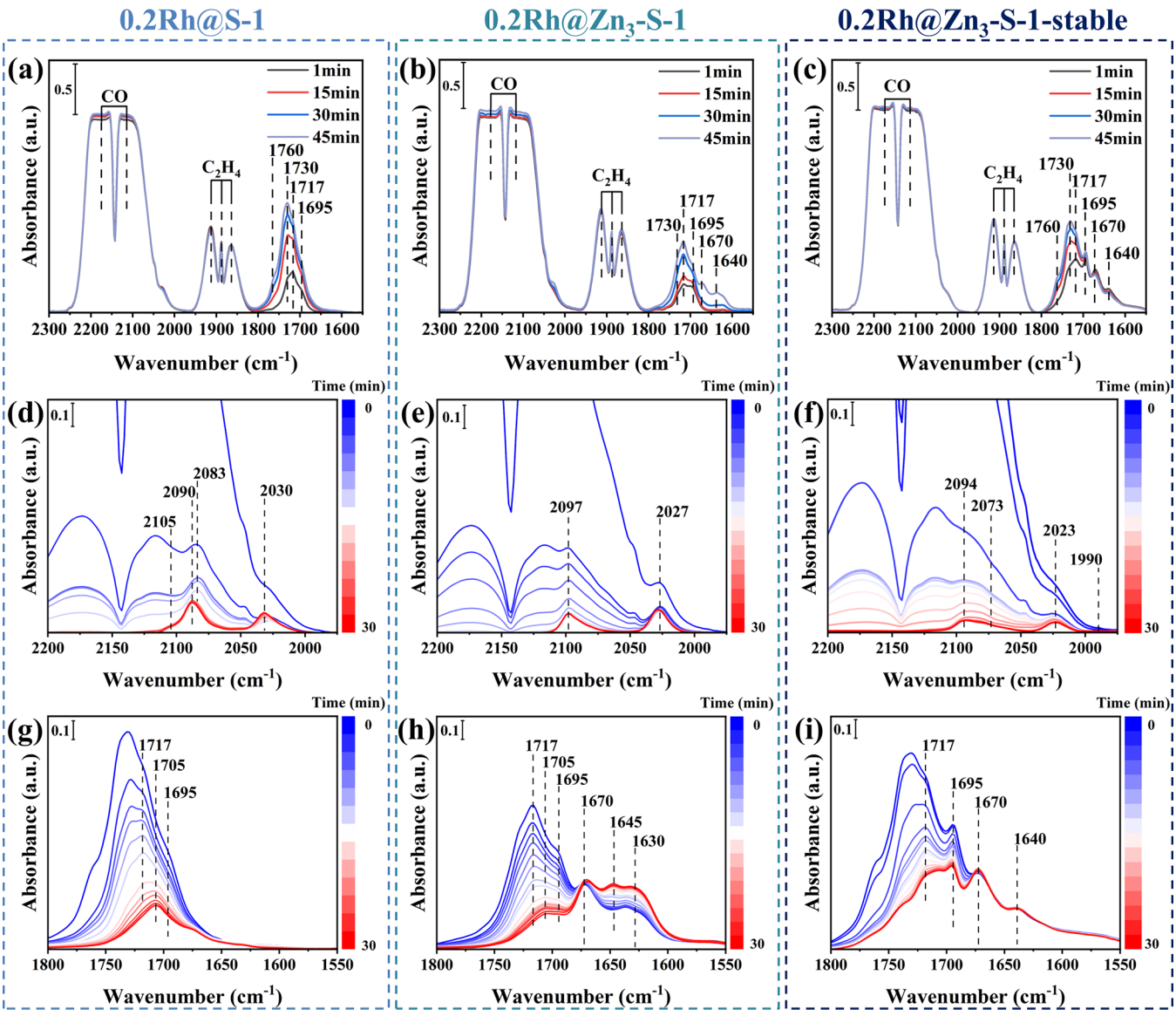

Figure 5. *In situ* FTIR spectra of (a) 0.2Rh@S-1, (b) 0.2Rh@Zn_3-S-1, and (c) 0.2Rh@Zn_3-S-1-stable during ethylene hydroformylation. Reaction conditions: 15 mg of the catalyst, 363 K, 1 MPa, feed gas $1C_2H_4/1H_2/1CO$, 30 mL(NTP)/min. FTIR spectra in the ranges of (d–f) 2200–1975 and (g–i) 1800–1550 cm^{-1} for 0.2Rh@S-1, 0.2Rh@Zn_3-S-1, and 0.2Rh@Zn_3-S-1-stable after the reaction followed by depressurization (1 MPa→0.1 MPa) of the spectroscopic cell and further argon flow purging for 30 min at 363 K.

coordination environments of Rh centers are reconstructed to be more uniform after the redispersion during the induction period.

The coordination number (CN) information on different Rh/Zn scattering paths for the catalysts was obtained from EXAFS fitting analysis. The fitting results and the corresponding fitting CNs are shown in Figures S25 and S26 as well as Tables S5–S6. For 0.2Rh@S-1, the CN of the Rh–O–Rh bond is 1.7 ± 0.6, illustrating that most of the Rh species are highly dispersed. However, for 0.2Rh@Zn_3-S-1, the CN of Rh–O–Rh (3.4 ± 1.0) is higher. After the induction period, the CN of Rh–O–Rh for 0.2Rh@Zn_3-S-1-stable drop to 1.9 ± 0.7, much lower than that for fresh 0.2Rh@Zn_3-S-1. The EXAFS data agree well with the HAADF-STEM and CO-adsorbed FTIR results. The XAS results further confirm the redispersion of Rh species in 0.2Rh@Zn_3-S-1 after the reaction induction period. Moreover, considering the well-improved catalytic stability of 0.2Rh@Zn_3-S-1-stable, the observed shorter Rh–O distance suggests the generation of a new Rh–$(O–Zn)_x$ structure.

Previous reports have indicated that the dispersion behavior of Rh is a complicated process, which can be triggered by either the reactant gas of CO, H_2, and olefins or the aldehyde products.[32,75] To figure out the motivation of Rh redispersion in 0.2Rh@Zn_3-S-1 during the induction period, the fresh sample was treated with different gases at 363 K for 6 h and then characterized by HAADF-STEM and tested for the hydroformylation reaction. From Figures S27–S30, it can be observed that the sample treated by CO shows Rh species with an average diameter of 1.3 nm, while the samples treated by H_2, C_2H_4, and syngas give larger average sizes of 2.1, 2.0, and 1.8 nm, respectively. Figure S31 presents the HAADF-STEM images of the fresh sample treated by the propanal product, showing that the average size of Rh nanoparticles increases to around 2.4 nm with large Rh nanoparticles (>3 nm) located on the external surface. A similar Rh aggregation phenomenon

https://doi.org/10.1021/jacs.5c07586
J. Am. Chem. Soc. 2025, 147, 34381–34394

induced by propanal treatment is also observed for Zn-free 0.2Rh@S-1, where the average Rh cluster diameter increases from 0.9 to 3.0 nm (Figures S18 and S32). The hydroformylation activity of these samples (Figure S33) is consistent with their Rh dispersions, and the samples pretreated with CO or syngas show an obviously shortened induction period. Considering that the particle size of Rh aggregates in fresh 0.2Rh@Zn_3-S-1 is around 2.0 nm (Figures 3d and S20), the redispersion of Rh particles during the reaction should result from the formation of mobile Rh-carbonyl species.[63,76−78] Moreover, the existence of Si−O−Zn−O(H) is speculated to be crucial for capturing Rh-carbonyl species, as CO was also reported to cause the agglomeration of Rh species.[32,63] Scheme 1 illustrates the proposed redispersion process of Rh species during the induction period, leading to the formation of stable and active Rh−$(O−Zn)_x$ sites.

A propanal tolerance test for 0.2Rh@Zn_3-S-1-stable was further conducted to verify the effect of the Rh−$(O−Zn)_x$ connection on preserving the Rh dispersion during catalysis. After a 6 h propanal/N_2 treatment, the size of Rh clusters remained almost unchanged (∼1.4 nm, Figure S34), evidencing the enhanced antiaggregation stability of Rh species imparted by Rh−$(O−Zn)_x$ structures. This phenomenon also demonstrates that the distribution and coordination environments of the Rh atoms in 0.2Rh@Zn_3-S-1-stable are uniform, and most of them should connect with Zn−O species.

Molecular dynamics (MD) simulations were conducted to elucidate the role of Si−O−Zn−O(H) in anchoring Rh-carbonyl species. As shown in Figure 4a, for Rh@S-1, no significant accumulation of Rh-carbonyl species can be discerned around Si−O (the region circled in light blue) in the simulation time of 400 and 800 ps. However, with the construction of the silanol-grafted Zn−O structures, the Rh-carbonyl species are obviously fixed around them (Figure 4b, the region circled in light yellow). The modeled coordination information between Si−O or Zn−O and Rh in Rh@S-1 and Rh@Zn_3-S-1 is presented in Figure 4c. A sharp and strong peak is observed at ca. 2.6 Å for Rh@Zn_3-S-1, while there is no peak observed for Rh@S-1 at the same distance. Considering the similar Rh−O−M bond (see Note S4 for details) distance in the EXAFS simulation results, this peak can be attributed to the bonding between Zn−O and Rh, proving that Zn−O has a strong anchoring effect on Rh-carbonyl species. The coordination information on Rh and O−Rh between Rh-carbonyl species is presented in Figure 4d. Both the models show a peak at ca. 3 Å, which represents the Rh−O−Rh interaction between different Rh-carbonyl molecules appearing in the channels of zeolites. However, the intensity of the peak for Rh@Zn_3-S-1 is weaker than that for Rh@S-1. The mean square displacements of Rh-carbonyl species during the 800 ps simulation time are presented in Figure 4e. It can be clearly seen that the movement of Rh-carbonyl species in Rh@S-1 is almost unhindered, while it is barely observable due to the anchoring effect of grafted Zn−O in Rh@Zn_3-S-1.

2.4. *In Situ* FTIR Analysis for the Surface Reaction Behavior during Hydroformylation. *In situ* FTIR spectra of 0.2Rh@S-1, 0.2Rh@Zn_3-S-1, and 0.2Rh@Zn_3-S-1-stable were recorded in stages of ethylene hydroformylation, postreaction depressurization, and further argon flow purging. Figure 5a−c present the FTIR spectra during hydroformylation. The bands associated with gas-phase CO (2250−2000 cm^{-1}) and gas-phase ethylene (1950−1820 cm^{-1}) dominate in the spectra,[79−81] which overlap the region of Rh-carbonyl species.[32,35] For 0.2Rh@S-1 (Figure 5a), the bands related to the reaction products and the intermediate appear at 1730, 1717, and 1695 cm^{-1}, which are observed since the beginning of the reaction and can be assigned to the C═O vibration of weakly adsorbed propanal on zeolite,[32] propanal adsorbed on $Rh^{\delta+}$,[32,35,82] and the Rh-propionyl intermediate,[83,84] respectively. The band at 1730 cm^{-1} intensifies over time, together with the appearance of a shoulder at 1760 cm^{-1}. The latter can be attributed to the C═O vibration of gas-phase propanal (Figure S35). For 0.2Rh@Zn_3-S-1, the changes in the *in situ* FTIR spectra within the first 30 min are similar to those of 0.2Rh@S-1, but two new bands appear at 1670 and 1640 cm^{-1} at 45 min (Figure 5b). However, for 0.2Rh@Zn_3-S-1-stable, the bands at 1670 and 1640 cm^{-1} can be observed at the beginning of the reaction (Figure 5c). They show little change with the prolonging of the reaction time, while the bands at 1760−1695 cm^{-1} rise progressively. Given the absence of the 1670 and 1640 cm^{-1} bands for Zn-free 0.2Rh@S-1, they are most likely related to propanal adsorbed on Zn species.

Figure 5d−f display the FTIR spectra in the Rh−CO region (2000−2100 cm^{-1}) during the fast depressurization and further argon purging. The spectra of 0.2Rh@S-1 (Figure 5d) show a band centered at 2083 cm^{-1} (Rh^{3+}−(CO)−propionyl[35]) during the fast gas-pressure release. This band shifts to 2090 cm^{-1} ($Rh^{+}(CO)_2$[22]) upon argon purging, with the appearance of a small shoulder at 2105 cm^{-1} (Rh^{3+}−CO[22,35]). This evolution can be attributed to the fast transformation of the Rh^{3+}−(CO)−propionyl intermediate to $Rh^{+}(CO)_2$.[35] Differently, the FTIR spectra of 0.2Rh@Zn_3-S-1 (Figure 5e) and 0.2Rh@Zn_3-S-1-stable (Figure 5f) only exhibit stable signals at 2097 and 2027 cm^{-1}, representing the $Rh^{\delta+}(CO)_2$ species. For 0.2Rh@Zn_3-S-1-stable, there exist additional weak bands at 2073 and 1990 cm^{-1}, which could be attributed to the symmetrical and asymmetrical stretching modes of $HRh(CO)_2$ species.[27,33] Meanwhile, the FTIR spectra in the 1800−1550 cm^{-1} region (Figure 5g−i) were also monitored to learn information on adsorbed carbonyl-containing species. For 0.2Rh@S-1 (Figure 5g), with the depressurization and argon purging, the intensity of the bands at 1717 cm^{-1} (Rh-propanal) and 1695 cm^{-1} (Rh-propionyl intermediate) decreases synchronously, while that of the band at 1705 cm^{-1} (propanal strongly adsorbed on Rh sites) is maintained. For 0.2Rh@Zn_3-S-1 (Figure 5h), as the intensity of the bands in the range of 1717−1695 cm^{-1} drops, those attributed to propanal adsorbed on Zn−O sites (1670−1630 cm^{-1}) increase. Considering the spatial proximity between Rh and Zn atoms in the formed Rh−$(O−Zn)_x$ structure, this change suggests the transfer of propanal from $Rh^{\delta+}$ sites to adjacent Zn−O sites, consistent with that observed in Figure 5b. However, for 0.2Rh@Zn_3-S-1-stable (Figure 5i), the intensity of the bands at 1670 and 1640 cm^{-1} does not change with the 1717 and 1695 cm^{-1} bands decreasing, implying that the Zn−O sites had been saturated by propanal when the catalyst reached the stable state. This phenomenon suggests stronger interactions between propanal and Zn−O sites. More evidence supporting the assignment of the bands of adsorbed propanal on Zn−O sites (1670−1640 cm^{-1}) can be found in Note S5 and Figures S36−S38.

To verify the above assignments of the bands, *in situ* FTIR spectra using ^{13}CO in the reaction mixture were recorded for 0.2Rh@Zn_3-S-1. As shown in Figures S39−S40, the bands associated with carbonyl species, including Rh-carbonyl species

https://doi.org/10.1021/jacs.5c07586
J. Am. Chem. Soc. 2025, 147, 34381−34394

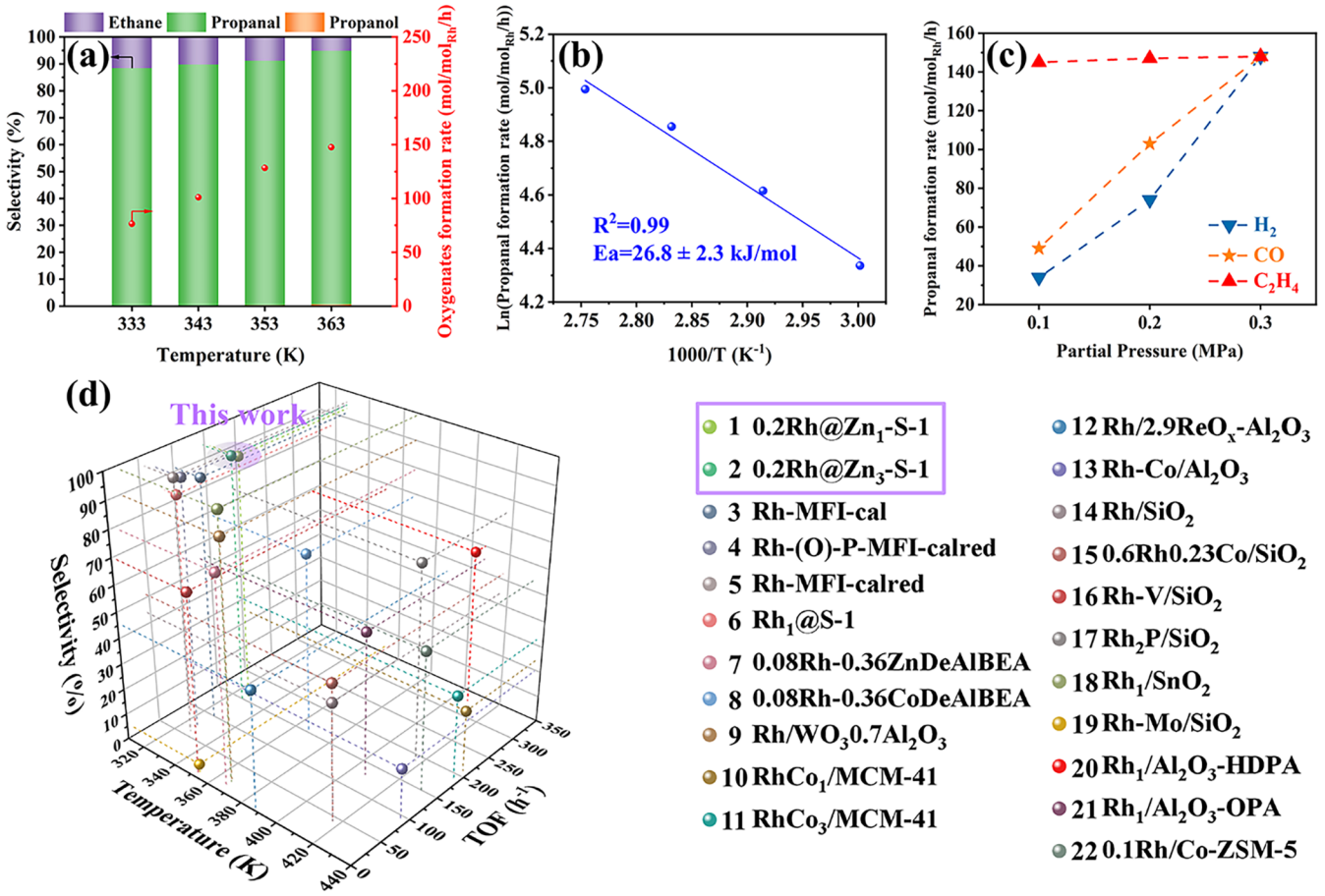

Figure 6. (a) Hydroformylation performance of 0.2Rh@Zn_3-S-1 under different temperatures in stable states. Reaction conditions: 1 MPa, a feed flow of $1C_2H_4/1H_2/1CO$ (30 mL(NTP)/min). (b) Apparent activation energy of 0.2Rh@Zn_3-S-1-stable. (c) Dependence of the propanal formation rate on the partial pressure of $CO/H_2/C_2H_4$ catalyzed by 0.2Rh@Zn_3-S-1-stable. Reaction conditions: 363 K, 1 MPa, a total flow of 30 mL(NTP)/min; feed gases: $1C_2H_4/1H_2/nCO/yN_2$ ($n + y = 1$), $1C_2H_4/xH_2/1CO/yN_2$ ($x + y = 1$), and $mC_2H_4/1H_2/1CO/yN_2$ ($m + y = 1$) for measuring the effect of the partial pressure of CO, H_2, and C_2H_4, respectively. (d) Comparison of the gas-phase ethylene hydroformylation performance among the catalysts in this work (highlighted in purple) and other state-of-the-art Rh-based catalysts. Detailed data are listed in Table S7.

(2000−2100 cm^{-1}), Rh-propionyl intermediates (1695 cm^{-1}), and propanal adsorbed on different sites (1640−1670, 1700−1730 cm^{-1}) all show a red shift of 40−50 cm^{-1}, confirming our assignments.

The FTIR results depicted the modulated hydroformylation reaction behavior from monometallic Rh to bimetallic Rh−$(O−Zn)_x$, which is reflected in both the reaction intermediate formation and the propanal product desorption. In the initial reaction stage, the strong interactions between Zn−O sites and propanal prompt the transfer of propanal from Rh sites, facilitating the mitigation of propanal-induced Rh aggregation (Figure 5b,h). Simultaneously, the Si−O−Zn−O(H) species on the framework interact with the volatile Rh species (e.g., Rh$(CO)_2$) to form a stable Rh−$(O−Zn)_x$ structure, achieving high Rh dispersion. During the steady-state reaction period, compared with 0.2Rh@S-1, the obvious band at 1695 cm^{-1} in the FTIR spectra of 0.2Rh@Zn_3-S-1-stable (Figure 5c) suggests a higher acyl intermediate formation rate relative to its conversion. The concurrent observation of $HRh(CO)_2$ species together with the high concentration of acyl intermediates indicates that the hydrogenation of acyl species should be the rate-limiting step of the hydroformylation reaction over 0.2Rh@Zn_3-S-1-stable.

2.5. Mechanism and Kinetic Discussion. The effects of the reaction temperature, total pressure, and gas hourly space velocity (GHSV) on the ethylene hydroformylation performance over 0.2Rh@Zn_3-S-1-stable were investigated. As shown in Figure 6a, increasing the temperature in the range of 333−363 K enhances both the propanal selectivity and the TOF. Moreover, the total pressure also exhibits a positive influence for the propanal selectivity and TOF (Figure S41a); as the pressure rises from 0.1 to 2 MPa, the TOF dramatically increases to 312 h^{-1} with the selectivity increasing to 97%. Data showing the influence of GHSV are presented in Figure S41b. When the GHSV increases from 9000 to 18,000 mL(NTP)/g_{cat}/h, the TOF remains almost unchanged, demonstrating that the catalysts were almost tested in the kinetic control range in this work (Figure 2). Additionally, the apparent activation energy for 0.2Rh@Zn_3-S-1-stable was determined to be 26.8 ± 2.3 kJ/mol (Figure 6b), which is much lower than those of typical Rh-supported catalysts (40−70 kJ/mol).[5,28,85−87] Similar apparent activation energies have been recently reported for Rh-(O)-P-MFI-calred (26.5 ± 2 kJ/mol)[35] and Rh-0.7W/Al_2O_3 (21 kJ/mol)[22] in gas-phase ethylene hydroformylation. These catalysts feature the same characteristics as 0.2Rh@Zn_3-S-1-stable, with $Rh^{\delta+}$ instead of Rh^0 as the active species.

https://doi.org/10.1021/jacs.5c07586
J. Am. Chem. Soc. 2025, 147, 34381−34394

In the kinetic study for ethylene hydroformylation, 0.2Rh@Zn_3-S-1-stable exhibits positive apparent reaction orders (k) for CO and H_2 (k_{CO} = 0.98, k_{H2} = 1.50) (Figures 6c and S42), similar to the results of 0.2Rh-MFI-cal and 0.2Rh-MFI-calred catalysts reported by Corma et al.[35] In contrast, the 0.08Rh-0.36Zn-DeAlBEA catalyst (k_{CO} = −1.1, k_{H2} = 1) reported by Bell et al.[5] exhibits an opposite CO pressure effect. We propose that this discrepancy arises primarily from the different valence states of Rh in these two catalysts. The electron transfer process from the d_π orbital of Rh to the p_{π^*} orbital of CO in the $\sigma-\pi$ Rh-carbonyl coordination complex can be influenced by the electron density of Rh centers.[88−90] When Rh is electron-rich Rh^0, this electron feedback process is more facile than that in the case of oxidized $Rh^{\delta+}$, resulting in a stronger CO binding to the Rh center. In 0.08Rh-0.36Zn-DeAlBEA, because of the pretreatment by H_2 under 473 K, the chemical state of Rh centers is inclined to be Rh^0, which causes the strong CO coordination and thus negative apparent reaction orders for CO. In contrast, the positively charged $Rh^{\delta+}$ centers in 0.2Rh@Zn_3-S-1 have weaker CO coordination, enabling the positive correlation between hydroformylation and CO partial pressure within the investigated range. The apparent reaction order to ethylene for 0.2Rh@Zn_3-S-1 is close to zero (Figure 6c), which differs from those of most Rh-containing catalysts but aligns with the Rh/S-1-OH catalyst (k_{C2H4} = 0.13) recently reported by Xiao et al.[91] They attributed this near-zero apparent reaction order to the enrichment effect of olefin molecules around Rh sites by silanol nests. Considering that silanol nests remain abundant in 0.2Rh@Zn_3-S-1 (Figure 1b), they may also facilitate ethylene enrichment.

The mechanism of Rh-catalyzed hydroformylation has been extensively studied through both experimental and theoretical studies.[16,28,92,93] The widely accepted pathway comprises the following steps: (1) ethylene reacting with Rh−H to form Rh-ethyl species, (2) CO insertion to generate Rh-acyl species, and (3) hydrogenation of Rh-acyl species to yield aldehydes. Building on these insights, the possible reaction pathways of 0.2Rh@Zn_3-S-1 in gas-phase ethylene hydroformylation are illustrated in Figure S43. The hydrogenation of the Rh-propionyl intermediates in 0.2Rh@Zn_3-S-1 is speculated to be the rate-limiting step, as deduced by the retention of the band at 1695 cm^{-1} in the argon-purged FTIR spectra (Figure 5i) and the higher apparent reaction order to H_2 (1.5).[5] This phenomenon is likely due to the fact that grafted Zn−O restricts the addition process of activated H to the Rh-propionyl intermediate.[20,22]

A comparison of the gas-phase ethylene hydroformylation performance among Rh-based solid catalysts is illustrated in Figure 6d. Notably, both 0.2Rh@Zn_1-S-1 and 0.2Rh@Zn_3-S-1 exhibit higher TOF values (159 and 148 h^{-1}, respectively) for carbonylation product formation compared to previously reported catalysts operating at low temperatures (<373 K).[32,35] For the Rh-supported catalysts operated at high temperatures (373−473 K), although their TOF for carbonylation products is higher, the selectivity is significantly inferior to those of 0.2Rh@Zn_1-S-1 (94%) and 0.2Rh@Zn_3-S-1 (95%). Furthermore, 0.2Rh@Zn_3-S-1 exhibits exceptional stability with no obvious signs of deactivation during the 40 h test, which is rarely achieved in gas-phase ethylene hydroformylation.

3. CONCLUSIONS

In summary, a series 0.2Rh@Zn_x-S-1 catalysts for gas-phase ethylene hydroformylation has been developed through the coencapsulation of Rh and Zn species into zeolite and *in situ* generation of Rh−$(O-Zn)_x$ sites during the reaction. The optimal Zn/Rh molar ratio is identified as 3, as Zn-insufficient samples (Zn/Rh = 0,1) exhibit an unstable hydroformylation performance, whereas Zn-overloaded samples (Zn/Rh = 5,10) show low carbonylation product TOF and selectivity due to the poor Rh dispersion and lack of $Rh^{\delta+}$. Characterization (STEM, XAS, FTIR) and MD simulations demonstrate that the capture of Rh-carbonyl species by Zn−O(H) grafted on the zeolite framework prompts the redispersion of Rh species to form $Rh^{\delta+}-(O-Zn)_x$. 0.2Rh@Zn_3-S-1 achieves a high propanal TOF of 148 h^{-1}, an oxygenate selectivity of 95%, and catalytic stability for over 40 h at a relatively low temperature (363 K), with a $C_2H_4/CO/H_2$ ratio of 1:1:1, surpassing most of the Rh-containing heterogeneous catalysts under comparable conditions. *In situ* FTIR experiments demonstrate that the constructed $Rh^{\delta+}-(O-Zn)_x$ sites lead to a higher generation rate of acyl intermediates relative to their conversion, with an additional observation of the $HRh(CO)_2$ species. In combination with the higher apparent reaction order to H_2 (1.5) observed in kinetics studies, the formation of propanal over 0.2Rh@Zn_3-S-1 is proposed to be rate-limited by the hydrogenation of $Rh^{\delta+}$-acyl intermediates. The insights gained from this investigation illustrate that the highly active $Rh^{\delta+}$ centers for low-temperature gas-phase hydroformylation can be stabilized by interactions with zeolite-framework-grafted Zn−O species.

■ ASSOCIATED CONTENT

Supporting Information

The Supporting Information is available free of charge at https://pubs.acs.org/doi/10.1021/jacs.5c07586.

Experimental section and additional data for catalyst characterization (SEM, XRD, BET, UV−vis, ICP, XPS, STEM, XAS, and FTIR) and reactions (PDF)

■ AUTHOR INFORMATION

Corresponding Authors

Liang Qi − *National Engineering Research Center of Lower-Carbon Catalysis Technology, Dalian National Laboratory for Clean Energy, Dalian Institute of Chemical Physics, Chinese Academy of Sciences, Dalian 116023, China;* orcid.org/0000-0002-2155-2061; Email: qlyanfei920@dicp.ac.cn

Peng Tian − *National Engineering Research Center of Lower-Carbon Catalysis Technology, Dalian National Laboratory for Clean Energy, Dalian Institute of Chemical Physics, Chinese Academy of Sciences, Dalian 116023, China;* orcid.org/0000-0002-8768-0154; Email: tianpeng@dicp.ac.cn

Zhongmin Liu − *National Engineering Research Center of Lower-Carbon Catalysis Technology, Dalian National Laboratory for Clean Energy, Dalian Institute of Chemical Physics, Chinese Academy of Sciences, Dalian 116023, China;* orcid.org/0000-0002-7999-2940; Email: liuzm@dicp.ac.cn

https://doi.org/10.1021/jacs.5c07586
J. Am. Chem. Soc. 2025, 147, 34381−34394

Authors

Haocheng Hu − *National Engineering Research Center of Lower-Carbon Catalysis Technology, Dalian National Laboratory for Clean Energy, Dalian Institute of Chemical Physics, Chinese Academy of Sciences, Dalian 116023, China; University of Chinese Academy of Sciences, Chinese Academy of Sciences, Beijing 100049, China*

Wenhao Cui − *Division of Energy Research Resources, Dalian Institute of Chemical Physics, Chinese Academy of Sciences, Dalian 116023, China*

Mingbin Gao − *State Key Laboratory of Physical Chemistry of Solid Surfaces, College of Chemistry and Chemical Engineering, Xiamen University, Xiamen 361005, China;* orcid.org/0000-0002-7143-2658

Linying Wang − *National Engineering Research Center of Lower-Carbon Catalysis Technology, Dalian National Laboratory for Clean Energy, Dalian Institute of Chemical Physics, Chinese Academy of Sciences, Dalian 116023, China*

Shiping Liu − *National Engineering Research Center of Lower-Carbon Catalysis Technology, Dalian National Laboratory for Clean Energy, Dalian Institute of Chemical Physics, Chinese Academy of Sciences, Dalian 116023, China*

Wenfu Yan − *State Key Laboratory of Inorganic Synthesis and Preparative Chemistry, College of Chemistry, Jilin University, Changchun 130012, China;* orcid.org/0000-0002-1000-6559

Complete contact information is available at: https://pubs.acs.org/10.1021/jacs.5c07586

Author Contributions

The manuscript was written through contributions of all authors. All authors have given approval to the final version of the manuscript.

Notes

The authors declare no competing financial interest.

■ ACKNOWLEDGMENTS

This work was supported by the National Key Research and Development Program of China (Grant No. 2024YFE0207000) and the National Natural Science Foundation of China (22288101, 22472173, and 22272173). L.Q. acknowledges the Youth Innovation Promotion Association, the Chinese Academy of Sciences (2023193).

■ REFERENCES

(1) Cole-Hamilton, D. J. Homogeneous Catalysis–New Approaches to Catalyst Separation, Recovery, and Recycling. *Science* **2003**, *299* (5613), 1702−1706.

(2) Franke, R.; Selent, D.; Börner, A. Applied Hydroformylation. *Chem. Rev.* **2012**, *112* (11), 5675−5732.

(3) Peng, J.-B.; Geng, H.-Q.; Wu, X.-F. The Chemistry of CO: Carbonylation. *Chem* **2019**, *5* (3), 526−552.

(4) Zeng, G.; Liang, K.; Huang, Y.; Liu, C.; Chen, H.; Wang, D.; Ma, J.; Dong, Z. Rh nanoparticles anchored on phosphorous-doped porous carbon for efficiently catalytic hydroformylation of alkenes. *Mol. Catal.* **2023**, *550*, No. 113548.

(5) Qi, L.; Das, S.; Zhang, Y.; Nozik, D.; Gates, B. C.; Bell, A. T. Ethylene Hydroformylation Catalyzed by Rhodium Dispersed with Zinc or Cobalt in Silanol Nests of Dealuminated Zeolite Beta. *J. Am. Chem. Soc.* **2023**, *145* (5), 2911−2929.

(6) Dou, X.; Yan, T.; Qian, L.; Hou, H.; Lopez-Haro, M.; Marini, C.; Agostini, G.; Meira, D. M.; Zhang, X.; Zhang, L.; Cao, Z.; Liu, L. Regioselective Hydroformylation with Subnanometre Rh Clusters in MFI Zeolite. *Nat. Catal.* **2024**, *7*, 666−667.

(7) Liu, B.; Huang, N.; Wang, Y.; Lan, X.; Wang, T. Promotion of Inorganic Phosphorus on Rh Catalysts in Styrene Hydroformylation: Geometric and Electronic Effects. *ACS Catal.* **2021**, *11* (3), 1787−1796.

(8) Clark, T. P.; Landis, C. R.; Freed, S. L.; Klosin, J.; Abboud, K. A. Highly Active, Regioselective, and Enantioselective Hydroformylation with Rh Catalysts Ligated by Bis-3,4-diazaphospholanes. *J. Am. Chem. Soc.* **2005**, *127* (14), 5040−5042.

(9) Navidi, N.; Thybaut, J. W.; Marin, G. B. Experimental investigation of ethylene hydroformylation to propanal on Rh and Co based catalysts. *Appl. Catal., A* **2014**, *469*, 357−366.

(10) Amsler, J.; Sarma, B. B.; Agostini, G.; Prieto, G.; Plessow, P. N.; Studt, F. Prospects of Heterogeneous Hydroformylation with Supported Single Atom Catalysts. *J. Am. Chem. Soc.* **2020**, *142* (11), 5087−5096.

(11) Liu, B.; Wang, Y.; Huang, N.; Lan, X.; Xie, Z.; Chen, J. G.; Wang, T. Heterogeneous hydroformylation of alkenes by Rh-based catalysts. *Chem* **2022**, *8* (10), 2630−2658.

(12) Delolo, F. G.; dos Santos, E. N.; Gusevskaya, E. V. Anisole: a further step to sustainable hydroformylation. *Green Chem.* **2019**, *21* (5), 1091−1098.

(13) Fan, B.; Jiang, M.; Wang, G.; Zhao, Y.; Mei, B.; Han, J.; Ma, L.; Li, C.; Hou, G.; Wu, T.; Yan, L.; Ding, Y. Elucidation of hemilabile-coordination-induced tunable regioselectivity in single-site Rh-catalyzed heterogeneous hydroformylation. *Nat. Commun.* **2024**, *15* (1), No. 6967.

(14) Wang, Y.; Yan, L.; Li, C.; Jiang, M.; Zhao, Z.; Hou, G.; Ding, Y. Heterogeneous Rh/CPOL-BP&P$(OPh)_3$ catalysts for hydroformylation of 1-butene: The formation and evolution of the active species. *J. Catal.* **2018**, *368*, 197−206.

(15) Rupflin, L. A.; Mormul, J.; Lejkowski, M.; Titlbach, S.; Papp, R.; Gläser, R.; Dimitrakopoulou, M.; Huang, X.; Trunschke, A.; Willinger, M. G.; Schlögl, R.; Rosowski, F.; Schunk, S. A. Platinum Group Metal Phosphides as Heterogeneous Catalysts for the Gas-Phase Hydroformylation of Small Olefins. *ACS Catal.* **2017**, *7* (5), 3584−3590.

(16) Liu, B.; Huang, N.; Wang, Y.; Lan, X.; Wang, T. Insights into the Activity Screening and Hydroformylation Kinetics of Rh-Based Bimetallic Phosphides. *ACS Catal.* **2021**, *11* (24), 15235−15243.

(17) Marinkovic, J. M.; Riisager, A.; Franke, R.; Wasserscheid, P.; Haumann, M. Fifteen Years of Supported Ionic Liquid Phase-Catalyzed Hydroformylation: Material and Process Developments. *Ind. Eng. Chem. Res.* **2019**, *58* (7), 2409−2420.

(18) Coufourier, S.; Gaillard, S.; Clet, G.; Serre, C.; Daturi, M.; Renaud, J.-L. A MOF-assisted phosphine free bifunctional iron complex for the hydrogenation of carbon dioxide, sodium bicarbonate and carbonate to formate. *Chem. Commun.* **2019**, *55* (34), 4977−4980.

(19) Gadge, S. T.; Bhanage, B. M. Recent developments in palladium catalysed carbonylation reactions. *RSC Adv.* **2014**, *4* (20), 10367−10389.

(20) Lee, S.; Patra, A.; Christopher, P.; Vlachos, D. G.; Caratzoulas, S. Theoretical Study of Ethylene Hydroformylation on Atomically Dispersed Rh/Al_2O_3 Catalysts: Reaction Mechanism and Influence of the ReO_x Promoter. *ACS Catal.* **2021**, *11* (15), 9506−9518.

(21) Ro, I.; Xu, M.; Graham, G. W.; Pan, X.; Christopher, P. Synthesis of Heteroatom Rh−ReO_x Atomically Dispersed Species on Al_2O_3 and Their Tunable Catalytic Reactivity in Ethylene Hydroformylation. *ACS Catal.* **2019**, *9* (12), 10899−10912.

(22) Ro, I.; Qi, J.; Lee, S.; Xu, M.; Yan, X.; Xie, Z.; Zakem, G.; Morales, A.; Chen, J. G.; Pan, X.; Vlachos, D. G.; Caratzoulas, S.; Christopher, P. Bifunctional hydroformylation on heterogeneous Rh-WO_x pair site catalysts. *Nature* **2022**, *609* (7926), 287−292.

(23) Lang, R.; Li, T.; Matsumura, D.; Miao, S.; Ren, Y.; Cui, Y.-T.; Tan, Y.; Qiao, B.; Li, L.; Wang, A.; Wang, X.; Zhang, T. Hydroformylation of Olefins by a Rhodium Single-Atom Catalyst with Activity Comparable to RhCl$(PPh_3)_3$. *Angew. Chem., Int. Ed.* **2016**, *55* (52), 16054−16058.

(24) Chen, M.; Gupta, G.; Ordonez, C. W.; Lamkins, A. R.; Ward, C. J.; Abolafia, C. A.; Zhang, B.; Roling, L. T.; Huang, W. Intermetallic Nanocatalyst for Highly Active Heterogeneous Hydroformylation. *J. Am. Chem. Soc.* **2021**, *143* (49), 20907−20915.
(25) Ichikawa, M.; Lang, A. J.; Shriver, D. F.; Sachtler, W. M. H. Selective hydroformylation of ethylene on rhodium-zinc-silica. An apparent example of site isolation of rhodium and Lewis acid-promoted carbonyl insertion. *J. Am. Chem. Soc.* **1985**, *107* (24), 7216−7218.
(26) Trunschke, A.; Böttcher, H.-C.; Fukuoka, A.; Ichikawa, M.; Miessner, H. Olefin hydroformylation and selective hydrogenation of acetaldehyde on Mo-promoted Rh/SiO_2 catalysts derived from metal salt and heteronuclear cluster precursors. *Catal. Lett.* **1991**, *8* (2), 221−228.
(27) Zheng, Y.; Wang, Q.; Yang, Q.; Wang, S.; Hülsey, M. J.; Ding, S.; Furukawa, S.; Li, M.; Yan, N.; Ma, X. Boosting the Hydroformylation Activity of a Rh/CeO_2 Single-Atom Catalyst by Tuning Surface Deficiencies. *ACS Catal.* **2023**, *13* (11), 7243−7255.
(28) Huang, N.; Liu, B.; Lan, X.; Wang, T. Insights into the Bimetallic Effects of a RhCo Catalyst for Ethylene Hydroformylation: Experimental and DFT Investigations. *Ind. Eng. Chem. Res.* **2020**, *59* (42), 18771−18780.
(29) Liu, B.; Huang, N.; Wang, Y.; Lan, X.; Wang, T. Promotion of Inorganic Phosphorus on Rh Catalysts In Styrene Hydroformylation: Geometric and Electronic Effects. *ACS Catal.* **2021**, *11* (3), 1787−1796.
(30) Xie, Z.; Xu, Y.; Xie, M.; Chen, X.; Lee, J. H.; Stavitski, E.; Kattel, S.; Chen, J. G. Reactions of CO_2 and ethane enable CO bond insertion for production of C3 oxygenates. *Nat. Commun.* **2020**, *11* (1), No. 1887.
(31) Chen, M.; Gupta, G.; Ordonez, C. W.; Lamkins, A. R.; Ward, C. J.; Abolafia, C. A.; Zhang, B.; Roling, L. T.; Huang, W. Intermetallic nanocatalyst for highly active heterogeneous hydroformylation. *J. Am. Chem. Soc.* **2021**, *143* (49), 20907−20915.
(32) Yu, Z.; Zhang, S.; Zhang, L.; Liu, X.; Jia, Z.; Li, L.; Ta, N.; Wang, A.; Liu, W.; Wang, A.; Zhang, T. Suppressing Metal Leaching and Sintering in Hydroformylation Reaction by Modulating the Coordination of Rh Single Atoms with Reactants. *J. Am. Chem. Soc.* **2024**, *146* (17), 11955−11967.
(33) Zhang, X.; Yan, T.; Hou, H.; Yin, J.; Wan, H.; Sun, X.; Zhang, Q.; Sun, F.; Wei, Y.; Dong, M.; Fan, W.; Wang, J.; Sun, Y.; Zhou, X.; Wu, K.; Yang, Y.; Li, Y.; Cao, Z. Regioselective hydroformylation of propene catalysed by rhodium-zeolite. *Nature* **2024**, *629*, 597−602.
(34) Zhang, J.; Sun, P.; Gao, G.; Wang, J.; Zhao, Z.; Muhammad, Y.; Li, F. Enhancing regioselectivity via tuning the microenvironment in heterogeneous hydroformylation of olefins. *J. Catal.* **2020**, *387*, 196−206.
(35) Zhao, M.; Li, C.; Gómez, D.; Gonell, F.; Diaconescu, V. M.; Simonelli, L.; Haro, M. L.; Calvino, J. J.; Meira, D. M.; Concepción, P.; Corma, A. Low-temperature hydroformylation of ethylene by phosphorous stabilized Rh sites in a one-pot synthesized Rh-(O)-P-MFI zeolite. *Nat. Commun.* **2023**, *14* (1), No. 7174.
(36) Shang, W.; Qin, B.; Gao, M.; Qin, X.; Chai, Y.; Wu, G.; Guan, N.; Ma, D.; Li, L. Efficient Heterogeneous Hydroformylation over Zeolite-Encaged Isolated Rhodium Ions. *CCS Chem.* **2023**, *5* (7), 1526−1539.
(37) Qu, Z.; He, G.; Zhang, T.; Fan, Y.; Guo, Y.; Hu, M.; Xu, J.; Ma, Y.; Zhang, J.; Fan, W.; Sun, Q.; Mei, D.; Yu, J. Tricoordinated Single-Atom Cobalt in Zeolite Boosting Propane Dehydrogenation. *J. Am. Chem. Soc.* **2024**, *146* (13), 8939−8948.
(38) Han, S. W.; Park, H.; Han, J.; Kim, J.-C.; Lee, J.; Jo, C.; Ryoo, R. PtZn Intermetallic Compound Nanoparticles in Mesoporous Zeolite Exhibiting High Catalyst Durability for Propane Dehydrogenation. *ACS Catal.* **2021**, *11* (15), 9233−9241.
(39) Zhang, B.; Li, G.; Zhai, Z.; Chen, D.; Tian, Y.; Yang, R.; Wang, L.; Zhang, X.; Liu, G. PtZn intermetallic nanoalloy encapsulated in silicalite-1 for propane dehydrogenation. *AIChE J.* **2021**, *67* (7), No. e17295.
(40) Chen, S.; Zhao, Z.-J.; Mu, R.; Chang, X.; Luo, J.; Purdy, S. C.; Kropf, A. J.; Sun, G.; Pei, C.; Miller, J. T.; Zhou, X.; Vovk, E.; Yang, Y.; Gong, J. Propane Dehydrogenation on Single-Site $[PtZn_4]$ Intermetallic Catalysts. *Chem* **2021**, *7* (2), 387−405.
(41) Liu, H.; Zhou, J.; Chen, T.; Hu, P.; Xiong, C.; Sun, Q.; Chen, S.; Lo, T. W. B.; Ji, H. Isolated Pt Species Anchored by Hierarchical-like Heteroatomic Fe-Silicalite-1 Catalyze Propane Dehydrogenation near the Thermodynamic Limit. *ACS Catal.* **2023**, *13* (5), 2928−2936.
(42) Bai, P.; Zhao, Z.; Zhang, Y.; He, Z.; Liu, Y.; Wang, C.; Ma, S.; Wu, P.; Zhao, L.; Mintova, S.; Yan, Z. Rational Design of Highly Efficient $PdIn-In_2O_3$ Interfaces by a Capture-Alloying Strategy for Benzyl Alcohol Partial Oxidation. *ACS Appl. Mater. Interfaces* **2023**, *15* (15), 19653−19664.
(43) Ryoo, R.; Kim, J.; Jo, C.; Han, S. W.; Kim, J.-C.; Park, H.; Han, J.; Shin, H. S.; Shin, J. W. Rare-earth−platinum alloy nanoparticles in mesoporous zeolite for catalysis. *Nature* **2020**, *585* (7824), 221−224.
(44) Ma, Y.; Song, S.; Liu, C.; Liu, L.; Zhang, L.; Zhao, Y.; Wang, X.; Xu, H.; Guan, Y.; Jiang, J.; Song, W.; Han, Y.; Zhang, J.; Wu, P. Germanium-enriched double-four-membered-ring units inducing zeolite-confined subnanometric Pt clusters for efficient propane dehydrogenation. *Nat. Catal.* **2023**, *6* (6), 506−518.
(45) Zeng, L.; Cheng, K.; Sun, F.; Fan, Q.; Li, L.; Zhang, Q.; Wei, Y.; Zhou, W.; Kang, J.; Zhang, Q.; Chen, M.; Liu, Q.; Zhang, L.; Huang, J.; Cheng, J.; Jiang, Z.; Fu, G.; Wang, Y. Stable anchoring of single rhodium atoms by indium in zeolite alkane dehydrogenation catalysts. *Science* **2024**, *383*, 998−1004.
(46) Wang, L.; Sang, S.; Meng, S.; Zhang, Y.; Qi, Y.; Liu, Z. Direct synthesis of Zn-ZSM-5 with novel morphology. *Mater. Lett.* **2007**, *61* (8), 1675−1678.
(47) Zhang, Y.; Zhou, Y.; Huang, L.; Zhou, S.; Sheng, X.; Wang, Q.; Zhang, C. Structure and catalytic properties of the Zn-modified ZSM-5 supported platinum catalyst for propane dehydrogenation. *Chem. Eng. J.* **2015**, *270*, 352−361.
(48) Su, X.; Hu, Z.-P.; Han, J.; Jia, Y.; Xu, S.; Zhang, J.; Fan, D.; Wei, Y.; Liu, Z. Biomolecule-inspired synthesis of framework zinc in MFI zeolite for propane dehydrogenation. *Microporous Mesoporous Mater.* **2023**, *348*, No. 112371.
(49) Chen, C.; Hu, Z.; Ren, J.; Zhang, S.; Wang, Z.; Yuan, Z.-Y. ZnO Nanoclusters Supported on Dealuminated Zeolite β as a Novel Catalyst for Direct Dehydrogenation of Propane to Propylene. *ChemCatChem* **2019**, *11* (2), 868−877.
(50) Sun, X.; Liu, R.; Fan, G.; Liu, Y.; Ye, F.; Yu, Z.; Liu, Z. Understanding the correlation between zinc speciation and coupling conversion of CO_2 and *n*-butane on zinc/ZSM-5 catalysts. *Chin. J. Catal.* **2024**, *61*, 154−163.
(51) Qi, L.; Babucci, M.; Zhang, Y.; Lund, A.; Liu, L.; Li, J.; Chen, Y.; Hoffman, A. S.; Bare, S. R.; Han, Y.; Gates, B. C.; Bell, A. T. Propane Dehydrogenation Catalyzed by Isolated Pt Atoms in ≡SiOZn−OH Nests in Dealuminated Zeolite Beta. *J. Am. Chem. Soc.* **2021**, *143* (50), 21364−21378.
(52) Karbowiak, T.; Saada, M. A.; Rigolet, S.; Ballandras, A.; Weber, G.; Bezverkhyy, I.; Soulard, M.; Patarin, J.; Bellat, J. P. New insights in the formation of silanol defects in silicalite-1 by water intrusion under high pressure. *Phys. Chem. Chem. Phys.* **2010**, *12* (37), 11454−11466.
(53) Liu, J.; Liu, Y.; Liu, H. C.; Fu, Y.; Chen, Z. Y.; Zhu, W. L. Silicalite-1 Supported ZnO as an Efficient Catalyst for Direct Propane Dehydrogenation. *ChemCatChem* **2021**, *13* (22), 4780−4786.
(54) Tang, B.; Dai, W. L.; Wu, G. J.; Guan, N. J.; Li, L. D.; Hunger, M. Improved Postsynthesis Strategy to Sn-Beta Zeolites as Lewis Acid Catalysts for the Ring-Opening Hydration of Epoxides. *ACS Catal.* **2014**, *4* (8), 2801−2810.
(55) Zhang, Y.; Qi, L.; Nozik, D.; Dun, C.; Urban, J. J.; Bell, A. T. Mechanism and Kinetics of Propane and n-Butane Dehydrogenation over Isolated and Nested ≡SiOZn−OH Sites Grafted onto Silanol Nests of Dealuminated Beta Zeolite. *ACS Catal.* **2024**, *14* (4), 2787−2804.
(56) Qi, L.; Zhang, Y. F.; Conrad, M. A.; Russell, C. K.; Miller, J.; Bell, A. T. Ethanol Conversion to Butadiene over Isolated Zinc and

Yttrium Sites Grafted onto Dealuminated Beta Zeolite. *J. Am. Chem. Soc.* **2020**, *142* (34), 14674−14687.
(57) Zhang, Y. F.; Qi, L.; Lund, A.; Lu, P.; Bell, A. T. Mechanism and Kinetics of Acetone Conversion to Isobutene over Isolated Hf Sites Grafted to Silicalite-1 and SiO_2. *J. Am. Chem. Soc.* **2021**, *143* (22), 8352−8366.
(58) Janiszewska, E.; Macario, A.; Wilk, J.; Aloise, A.; Kowalak, S.; Nagy, J. B.; Giordano, G. The role of the defect groups on the Silicalite-1 zeolite catalytic behavior. *Microporous Mesoporous Mater.* **2013**, *182*, 220−228.
(59) Palčić, A.; Moldovan, S.; El Siblani, H.; Vicente, A.; Valtchev, V. Defect Sites in Zeolites: Origin and Healing. *Adv. Sci.* **2022**, *9*, No. 2104414.
(60) Liu, D.; Liu, L.; Wu, K.; Zhou, J.; Cheng, Q.; Lv, J.; Cao, T.; Zhang, D.; Lin, F.; Han, Y. Possible Misidentification of Heteroatom Species in Scanning Transmission Electron Microscopy Imaging of Zeolites. *J. Phys. Chem. C* **2021**, *125* (34), 18952−18960.
(61) Medeiros-Costa, I. C.; Dib, E.; Nesterenko, N.; Dath, J. P.; Gilson, J. P.; Mintova, S. Silanol defect engineering and healing in zeolites: opportunities to fine-tune their properties and performances. *Chem. Soc. Rev.* **2021**, *50* (19), 11156−11179.
(62) Bordiga, S.; Roggero, I.; Ugliengo, P.; Zecchina, A.; Bolis, V.; Artioli, G.; Buzzoni, R.; Marra, G.; Rivetti, F.; Spanò, G.; Lamberti, C. Characterisation of defective silicalites. *J. Chem. Soc., Faraday Trans. 1* **2000**, No. 21, 3921−3929.
(63) Zakem, G.; Christopher, P. Active Site Entropy of Atomically Dispersed Rh/Al_2O_3 Catalysts Dictates Activity for Ethylene Hydroformylation. *ACS Catal.* **2023**, *13* (8), 5502−5515.
(64) Li, B.; Li, X.; Asami, K.; Fujimoto, K. Low-Pressure Hydroformylation of Middle Olefins over Co and Rh Supported on Active Carbon Catalysts. *Energy Fuels* **2003**, *17* (4), 810−816.
(65) Basu, P.; Panayotov, D.; Yates, J. T. Rhodium-carbon monoxide surface chemistry: the involvement of surface hydroxyl groups on alumina and silica supports. *J. Am. Chem. Soc.* **1988**, *110* (7), 2074−2081.
(66) Hoffman, A. S.; Fang, C.-Y.; Gates, B. C. Homogeneity of surface sites in supported single-site metal catalysts: assessment with band widths of metal carbonyl infrared spectra. *J. Phys. Chem. Lett.* **2016**, *7* (19), 3854−3860.
(67) Matsubu, J. C.; Yang, V. N.; Christopher, P. Isolated metal active site concentration and stability control catalytic CO_2 reduction selectivity. *J. Am. Chem. Soc.* **2015**, *137* (8), 3076−3084.
(68) Miessner, H.; Burkhardt, I.; Gutschick, D.; Zecchina, A.; Morterra, C.; Spoto, G. The formation of a well defined rhodium dicarbonyl in highly dealuminated rhodium-exchanged zeolite Y by interaction with CO. *J. Chem. Soc., Faraday Trans. 1* **1989**, *85* (8), 2113−2126.
(69) Stevenson, S. A.; Lisitsyn, A.; Knoezinger, H. Adsorption of carbon monoxide on manganese-promoted rhodium/silica catalysts as studied by infrared spectroscopy. *J. Phys. Chem. A* **1990**, *94* (4), 1576−1581.
(70) Zhang, Z.; Kladi, A.; Verykios, X. E. Spectroscopic study of the effects of carrier doping on the surface structure of Rh/TiO_2 catalysts and on their interaction with CO and H_2. *J. Phys. Chem. A* **1994**, *98* (27), 6804−6811.
(71) Li, B.; Gao, J.; Shao, J.; Geng, R.; Qin, Z.; Wang, J.; Fan, W.; Dong, M. A Fine Analysis of Zn Species Structure and Distribution in Zn/ZSM-5 Catalysts by Linear Combination Fitting Analysis of XANES Spectra. *Molecules* **2024**, *29* (3), No. 631.
(72) Mallette, A. J.; Hong, S.; Freeman, E. E.; Saslow, S. A.; Mergelsberg, S.; Motkuri, R. K.; Neeway, J. J.; Mpourmpakis, G.; Rimer, J. D. Heteroatom manipulation of zeolite crystallization: stabilizing Zn-FAU against interzeolite transformation. *JACS Au* **2022**, *2* (10), 2295−2306.
(73) Parmar, D.; Mallette, A. J.; Linares, N.; Saslow, S. A.; Terlier, T.; Strohm, J. J.; Barber, L. P.; Dai, H.; García-Martínez, J.; Rimer, J. D. Direct synthesis of highly siliceous ZnO-FAU zeolite with enhanced performance in hydrocarbon cracking reactions. *ACS Mater. Lett.* **2023**, *5* (1), 202−208.
(74) Yan, W.; Xi, S.; Du, Y.; Schreyer, M. K.; Tan, S. X.; Liu, Y.; Borgna, A. J. C. Heteroatomic Zn-MWW Zeolite Developed for Catalytic Dehydrogenation Reactions: A Combined Experimental and DFT Study. *ChemCatChem* **2018**, *10* (14), 3078−3085.
(75) Navidi, N.; Thybaut, J. W.; Marin, G. B. Experimental Investigation of ethylene hydroformylation to propanal on Rh and Co based catalysts. *Appl. Catal., A* **2014**, *469*, 357−366.
(76) Suzuki, A.; Inada, Y.; Yamaguchi, A.; Chihara, T.; Yuasa, M.; Nomura, M.; Iwasawa, Y. Time Scale and Elementary Steps of CO-Induced Disintegration of Surface Rhodium Clusters. *Angew. Chem., Int. Ed.* **2003**, *42* (39), 4795−4799.
(77) Yates, J. T., Jr; Duncan, T. M.; Worley, S. D.; Vaughan, R. W. Infrared spectra of chemisorbed CO on Rh. *J. Chem. Phys.* **1979**, *70* (3), 1219−1224.
(78) Cavanagh, R. R.; Yates, J. T. Site distribution studies of Rh supported on Al_2O_3—An infrared study of chemisorbed CO. *J. Chem. Phys.* **1981**, *74* (7), 4150−4155.
(79) Dartois, E. Infrared spectroscopy of clathrate hydrates for planetary science: the ethylene case. *Mon. Not. R. Astron. Soc.* **2021**, *504* (3), 4369−4376.
(80) Dreimann, J. M.; Kohls, E.; Warmeling, H. F. W.; Stein, M.; Guo, L. F.; Garland, M.; Dinh, T. N.; Vorholt, A. J. In situ infrared spectroscopy as a tool for monitoring molecular catalyst for hydroformylation in continuous processes. *ACS Catal.* **2019**, *9* (5), 4308−4319.
(81) Koch, D.; Leitner, W. Rhodium-catalyzed hydroformylation in supercritical carbon dioxide. *J. Am. Chem. Soc.* **1998**, *120* (51), 13398−13404.
(82) Nishiyama, S.; Hara, T.; Tsuruya, S.; Masai, M. Infrared Spectroscopy Study of Aldehydes Adsorbed on Rh−Sn Bimetallic Systems: Selective Activation of Aldehydes by Tin. *J. Phys. Chem. B* **1999**, *103* (21), 4431−4439.
(83) Sivasankar, N.; Frei, H. Direct observation of kinetically competent surface intermediates upon ethylene hydroformylation over Rh/Al_2O_3 under reaction conditions by time-resolved fourier transform infrared spectroscopy. *J. Phys. Chem. C* **2011**, *115* (15), 7545−7553.
(84) Haji, S.; Erkey, C. Investigation of rhodium catalyzed hydroformylation of ethylene in supercritical carbon dioxide by in situ FTIR spectroscopy. *Tetrahedron* **2002**, *58* (20), 3929−3941.
(85) Huang, L. Formation of bimetallic $RhCo_3$ clusters from monometallic carbonyl clusters on SiO_2 as probed by hydroformylation. *J. Mol. Catal. A:Chem.* **1997**, *125* (1), 47−52.
(86) Takahashi, N.; Kobayashi, M. Comparison of ethylene with propylene hydroformylation over a Rh-Y zeolite catalyst under atmospheric pressure. *J. Catal.* **1984**, *85* (1), 89−97.
(87) Takahashi, N.; Matsuo, H.; Kobayashi, M. Kinetics and mechanism of ethylene hydroformylation over Rh-Y zeolite under atmospheric pressure. *J. Chem. Soc., Faraday Trans. 1* **1984**, *80* (3), 629−634.
(88) Devarajan, D.; Gunnoe, T. B.; Ess, D. H. Theory of Late-Transition-Metal Alkyl and Heteroatom Bonding: Analysis of Pt, Ru, Ir, and Rh Complexes. *Inorg. Chem.* **2012**, *51* (12), 6710−6718.
(89) Musaev, D. G.; Morokuma, K. Structure, Stability, and Bonding of Transition-Metal−Boryl Complexes. A Molecular Orbital Study. *J. Phys. Chem. A* **1996**, *100* (16), 6509−6517.
(90) Furukawa, S.; Horike, N.; Kondo, M.; Hijikata, Y.; Carné-Sánchez, A.; Larpent, P.; Louvain, N.; Diring, S.; Sato, H.; Matsuda, R.; Kawano, R.; Kitagawa, S. Rhodium−Organic Cuboctahedra as Porous Solids with Strong Binding Sites. *Inorg. Chem.* **2016**, *55* (21), 10843−10846.
(91) Liu, Y.; Liu, Z.; Hui, Y.; Wang, L.; Zhang, J.; Yi, X.; Chen, W.; Wang, C.; Wang, H.; Qin, Y.; Song, L.; Zheng, A.; Xiao, F.-S. Rhodium nanoparticles supported on silanol-rich zeolites beyond the homogeneous Wilkinson's catalyst for hydroformylation of olefins. *Nat. Commun.* **2023**, *14* (1), No. 2531.
(92) Lee, S.; Patra, A.; Christopher, P.; Vlachos, D. G.; Caratzoulas, S. Theoretical Study of Ethylene Hydroformylation on Atomically

Dispersed Rh/Al_2O_3 Catalysts: Reaction mechanism and Influence of the ReO_x Promoter. *ACS Catal.* **2021**, *11* (15), 9506−9518.
(93) Mao, Z.; Xie, Z.; Chen, J. G. Comparison of Heterogeneous Hydroformylation of Ethylene and Propylene over $RhCo_3$/MCM-41 Catalysts. *ACS Catal.* **2021**, *11* (23), 14575−14585.

https://doi.org/10.1021/jacs.5c07586
J. Am. Chem. Soc. 2025, 147, 34381−34394